Advanced Functional Materials

ADVANCED FUNCTIONAL MATERIALS
www.afm-journal.de

RESEARCH ARTICLE

Atomically Sharp Heterophase Interfaces in Cation-Eutaxy A–III–V Compounds

Seungyeon Kim[1,2] | Jongbum Won[1,2] | Taeyoung Kim[1,2] | Hong Choi[1,2] | Seokmin Park[1,2] | Jinwoo Cheon[3,4,5] | Jae-Hyun Lee[4,5] | Young Jin Choi[6] | Wooyoung Shim[1,2,4,5]

[1]Department of Materials Science and Engineering, Yonsei University, Seoul, South Korea | [2]Center For Multi-Dimensional Materials, Yonsei University, Seoul, South Korea | [3]Department of Chemistry, Yonsei University, Seoul, South Korea | [4]Center For Nanomedicine, Institute For Basic Science (IBS), Seoul, South Korea | [5]Yonsei IBS Institute, Yonsei University, Seoul, South Korea | [6]Department of Nanotechnology and Advanced Materials Engineering, Hybrid Materials Research Center (HMC), Sejong University, Seoul, South Korea

Correspondence: Wooyoung Shim (wshim@yonsei.ac.kr)

Received: 13 December 2025 | **Revised:** 8 March 2026 | **Accepted:** 11 March 2026

Keywords: atomically sharp heterophase interface| cation-eutaxy A–III–V compound| wet etching

ABSTRACT

Atomically sharp interfaces between dissimilar crystal phases are typically achieved through vacuum-based epitaxial growth, whereas solution-based processes generally produce broadened reaction fronts and compositional gradients. Here, we show that wet etching of cation-eutaxy A–III–V compounds unexpectedly yields atomically sharp heterophase interfaces. Using $CaGa_2P_2$ as a model system, we demonstrate a composition-driven structural evolution from a stable cation-eutaxy phase to a metastable Ca-deficient cation-eutaxy phase, followed by the emergence of an atomically sharp interface between cation-eutaxy $CaGa_2P_2$ and zinc-blende GaP, and culminating in complete conversion to zinc-blende GaP. This behavior arises from the absence of thermodynamically stable intermediate phases, a large mixing enthalpy imposed by coordination mismatch, and strong curvature-driven interface flattening associated with directional III–V covalent bonding. The same transition pathway and atomic scale interface sharpness are reproduced in $CaIn_2P_2$ and $CaGa_2As_2$, establishing the generality of this mechanism across cation-eutaxy A–III–V compounds. These findings demonstrate that atomic-scale interface control is achievable in diffusion-limited solution processes and motivate future electrical and optical studies of devices exploiting such sharply defined heterophases.

1 | Introduction

Heterophases with atomically sharp interfaces are most commonly realized through epitaxial growth under high-vacuum conditions [1, 2]. In deposition-based processes, surface diffusion and lattice matching can be tightly regulated, allowing interfaces between dissimilar phases to be defined down to a single atomic layer. Wet etching, in contrast, represents a prototypical diffusion–reaction–limited process [3] in which the transport of dissolved species and surface dissolution occur simultaneously. As a result, local variations in defects, facet-dependent surface energies, and bond strengths typically give rise to spatially nonuniform dissolution rates [4]. These characteristics generally broaden the reaction front over several nanometers and produce extended compositional gradients [5], making atomically abrupt interfaces difficult to achieve through solution-based processing.

In this study, we demonstrate that atomically sharp heterophase interfaces can nonetheless form during wet etching of cation-eutaxy A–III–V compounds, specifically $CaGa_2P_2$, $CaIn_2P_2$, and

Seungyeon Kim, Jongbum Won, and Taeyoung Kim contributed equally to this work.

$CaGa_2As_2$. These materials consist of III–V layers alternating with intercalated A-site cations, forming a layered framework stabilized by cation eutaxy [6–8]. Complete removal of the A-site cation restores the III–V sublattice to its thermodynamically stable zinc-blende (ZB) structure. When regions in which the A cation remains coexist with regions in which it has been removed, a heterogeneous phase state necessarily emerges, generating an interface between the cation-eutaxy phase and the ZB III–V phase. The formation of such an interface at the single-atomic-layer scale constitutes an atomically sharp heterophase.

Solution-based topochemical etching selectively removes the interlayer cation located between III–V layers [9–12]. However, the reaction proceeds under conventional wet etching conditions in which the spatial location of the etching front is not externally controlled (Figure 1a). Despite this apparent lack of precision, the Ga–P, Ga–As, and In–P sublattices remain intact without long-range rearrangement. Once the Ca concentration locally falls below a critical composition, the newly formed ZB III–V phase emerges and directly contacts the residual cation-eutaxy framework within one to two atomic layers. This behavior stands in marked contrast to the reaction front broadening and compositional smoothing that are typically observed during wet etching.

The emergence of such atomically sharp interfaces can be understood by considering the intrinsic structural and thermodynamic characteristics of cation-eutaxy materials. First, the large coordination mismatch between the III–V polyhedra in the cation-eutaxy phase (Ga_2P_6, Ga_2As_6, In_2P_6) and the sp^3 tetrahedra of the ZB phase strongly increases the mixing enthalpy (ΔH_{mix}), thereby suppressing mutual solubility and confining compositional accommodation to the atomic scale [13]. Second, the strong covalent character of the III–V sublattice raises the energetic cost of bond angle and bond length distortions at the interface, leading to a large interfacial energy [14]. According to the Gibbs–Thomson relation [15], this high interfacial energy provides a strong driving force for curvature relaxation, promoting interface flattening. The combination of intrinsically low miscibility and curvature-driven interface smoothing enables atomically sharp interfaces to form even under diffusion-limited wet etching conditions.

2 | Results and Discussion

2.1 | Thermodynamic Pathway for Heterophase and Sharp Interface Formation During Ca Etching

The structural transition induced by selective Ca removal from $CaGa_2P_2$ can be rationalized by considering both formation enthalpy (ΔH_f) and Gibbs free energy (Figure 1b). According to the Ca–Ga–P phase diagram at T = 0 K (Figure 1b, bottom right inset), $CaGa_2P_2$ ($\Delta H_f = -0.797$ eVatom^{-1}) and ZB GaP ($\Delta H_f = -0.509$ eVatom^{-1}) represent the only thermodynamically stable phases at the two ends of the Ga:P = 1:1 tie line [16]. No equilibrium single phase exists for intermediate Ca-deficient compositions corresponding to $Ca_{1-x}Ga_2P_2$. Instead, in this compositional range, the thermodynamically stable state corresponds to a two-phase mixture of $CaGa_2P_2$ and ZB GaP on the 0 K convex hull, with the relative phase fractions determined by the lever rule along the tie-line. From the standpoint of ΔH_f, decreasing the Ca content therefore stabilizes a $CaGa_2P_2$/ZB GaP heterophase relative to a homogeneous Ca-deficient compound.

The initiation of the phase transition, however, is governed by the Gibbs free energy landscape and the associated activation barrier. The free energy of a Ca-deficient heterophase can be expressed as $G_{Hetero}(x) = (1-x)G_{CaGa_2P_2} + xG_{GaP} + G_{Interface}$, where $G_{CaGa_2P_2}$ and G_{GaP} are the bulk free energies of $CaGa_2P_2$ and ZB GaP, respectively, and $G_{Interface}$ represents the interfacial energy contribution. Because $CaGa_2P_2$ has a lower formation enthalpy and contains a larger number of atomic species, resulting in a higher configurational entropy contribution [17, 18], the inequality $G_{CaGa_2P_2} < G_{GaP}$ generally holds. As a consequence, the inclusion of the G_{GaP} term together with the positive $G_{Interface}$ term yields $G_{Hetero}(x) > G_{CaGa_2P_2}$, as illustrated in Figure 1b (top left inset).

Despite this thermodynamic preference, $H_{2x}Ca_{1-x}Ga_2P_2$ can persist as a metastable single phase over a finite composition range. Formation of the heterophase requires lattice reconstruction in which the Ga_2P_6 ethane-like motifs of $CaGa_2P_2$ rearrange into the sp^3 tetrahedral coordination characteristic of ZB GaP. This reconstruction involves a substantial activation energy [19], analogous to local lattice rearrangements reported for layered-to-spinel transitions during Li deintercalation [20, 21]. Consequently, even when the Ca concentration exceeds the thermodynamic stability limit, the cation-eutaxy framework can remain kinetically trapped, giving rise to a metastable Ca-deficient cation-eutaxy phase.

Once the two phases coexist, the interface must accommodate a sharp compositional discontinuity [22]. The thickness of this accommodation region is dictated by the miscibility between the two phases and the interfacial energy. The coordination mismatch between the Ga_2P_6 polyhedra of $CaGa_2P_2$ [23] and the GaP_4 tetrahedra of ZB GaP [24] produces a large ΔH_{mix}, generating a wide miscibility gap that confines the compositional transition to a few atomic layers (Figure 1c) [25]. At the same time, the strong covalent nature of the Ga–P sublattice leads to a high interfacial energy (γ) [26, 27]. The curvature-dependent chemical potential is given by $\mu(\kappa) = \mu_0 + \gamma\Omega\kappa$, where μ_0 is the chemical potential of a flat interface, Ω is the atomic volume, and κ is the curvature [15]. A large γ produces strong chemical potential gradients ($\nabla\mu$), which drive atomic fluxes according to $J = -M\nabla\mu$, where M is the atomic mobility. These fluxes rapidly reduce interfacial curvature, causing the interface to evolve toward a flat, atomically sharp configuration (Figure 1d). High-angle annular dark-field (HAADF)–scanning transmission electron microscopy (STEM) directly captures this curvature-driven interface evolution. At intermediate stages, the $CaGa_2P_2$/ZB GaP heterophase exhibits asymmetric interfaces with residual roughness, whereas at later stages both upper and lower interfaces become planar and are defined within a single atomic layer (Figure 1e,f).

2.2 | Atomic Scale Visualization of Ca Composition-Dependent Phase States in $CaGa_2P_2$

Wet etching removes Ca^{2+} through an aliovalent ion-exchange process in which Ca^{2+} in the solid is replaced by H^+. The Ca composition-dependent phase states in $CaGa_2P_2$ (Figure 2a) were

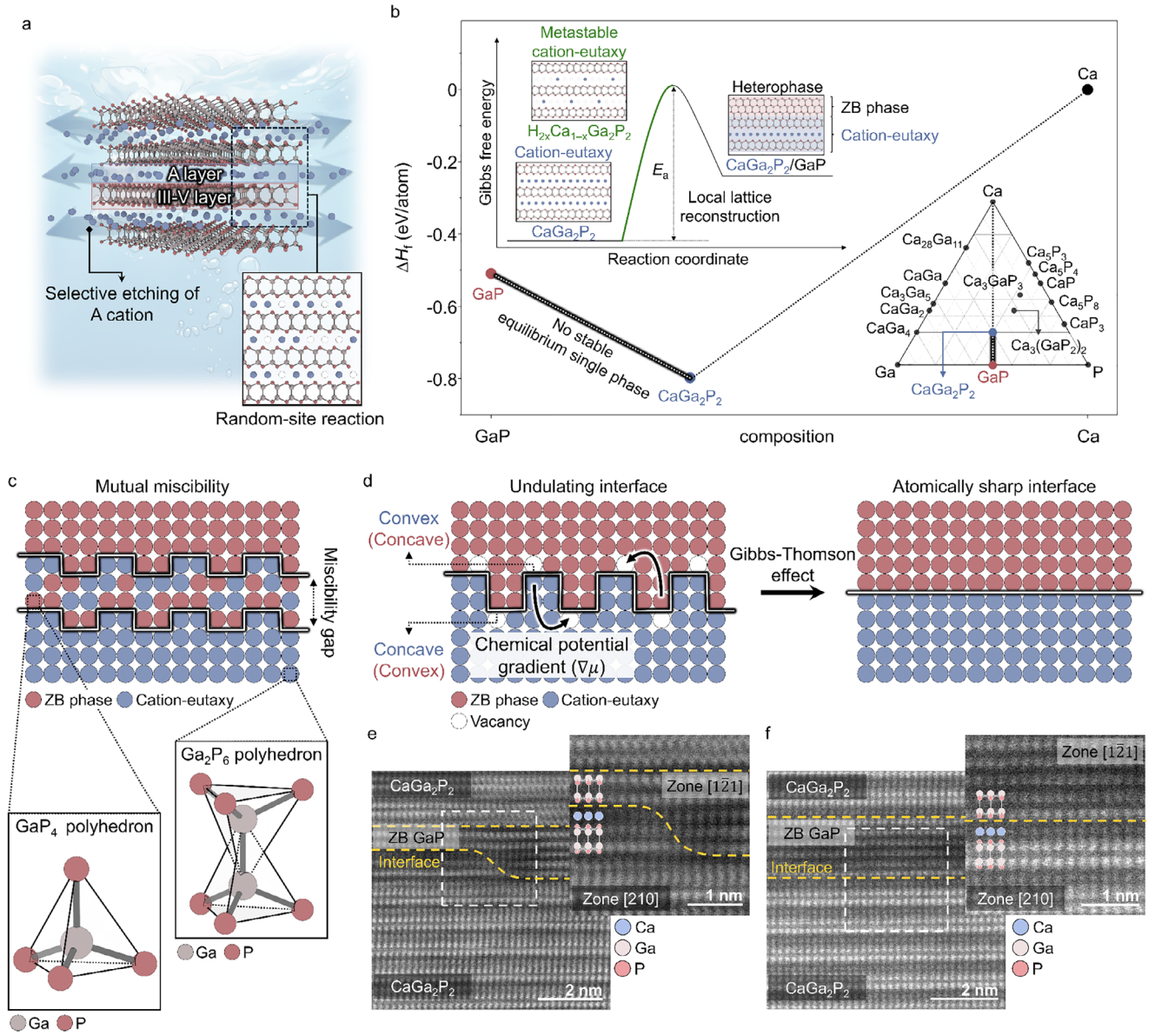

FIGURE 1 | Thermodynamic and structural origin of atomically sharp interfaces in $CaGa_2P_2$. (a) Schematic of solution-based topochemical Ca etching in cation-eutaxy A–III–V compounds, where Ca is selectively removed while the III–V framework remains intact. (b) Zero-kelvin Ca–Ga–P phase diagram (bottom right) and the ΔH_f landscape along the $CaGa_2P_2$–GaP tie-line. Along the Ga:P = 1:1 compositional line, $CaGa_2P_2$ and ZB GaP are the only ground-state stable phases, and no equilibrium single phase exists for intermediate Ca-deficient compositions ($Ca_{1-x}Ga_2P_2$). The straight line, therefore, represents the tie-line on the 0 K convex hull connecting these two phases. The top-left inset shows a schematic Gibbs free-energy curve, where lattice reconstruction introduces an activation barrier (E_a) that allows metastable retention of the cation-eutaxy phase prior to heterophase formation. (c) Coordination mismatch between the cation-eutaxy Ga_2P_6 motif and the ZB GaP_4 tetrahedron, restricting interfacial mixing to the atomic scale. (d) Curvature-driven interface flattening. High interfacial energy ($\gamma\gamma$) generates a chemical-potential gradient that relaxes an initially stepped boundary into a flat, atomically abrupt interface. (e,f) HAADF–STEM images showing a stepped intermediate interface (e) and a fully relaxed, atomically sharp $CaGa_2P_2$/ZB GaP interface (f). The inset shows an enlarged HAADF–STEM image of the area marked with a white box.

systematically examined by HAADF–STEM, with average compositions independently verified by scanning electron microscope (SEM)–energy dispersive X-ray spectroscopy (EDS) analysis (Figure S1). Pristine $CaGa_2P_2$ exists as a stable cation-eutaxy single phase. At intermediate Ca deficiency, two distinct structural states are observed. $H_{2x}Ca_{0.4}Ga_2P_2$ retains the cation-eutaxy framework but with reduced Ca occupancy, forming a metastable single phase. Charge imbalance induced by Ca removal can be compensated by protonation, allowing $H_{2x}Ca_{0.4}Ga_2P_2$ to retain the cation-eutaxy structure [6]. In contrast, $Ca_{0.3}Ga_2P_2$ exhibits coexistence of cation-eutaxy $CaGa_2P_2$ and ZB GaP, while near-complete Ca removal yields a ZB GaP single phase.

Along the [100] zone axis, pristine $CaGa_2P_2$ displays alternating Ca^{2+} layers and $[Ga_2P_2]^{2-}$ layers composed of two Ga planes and outer P planes (Figure 2b) [23]. The weak intensity of P columns reflects atomic number Z-contrast effects [28], and the atomic column arrangement matches the projected crystal structure.

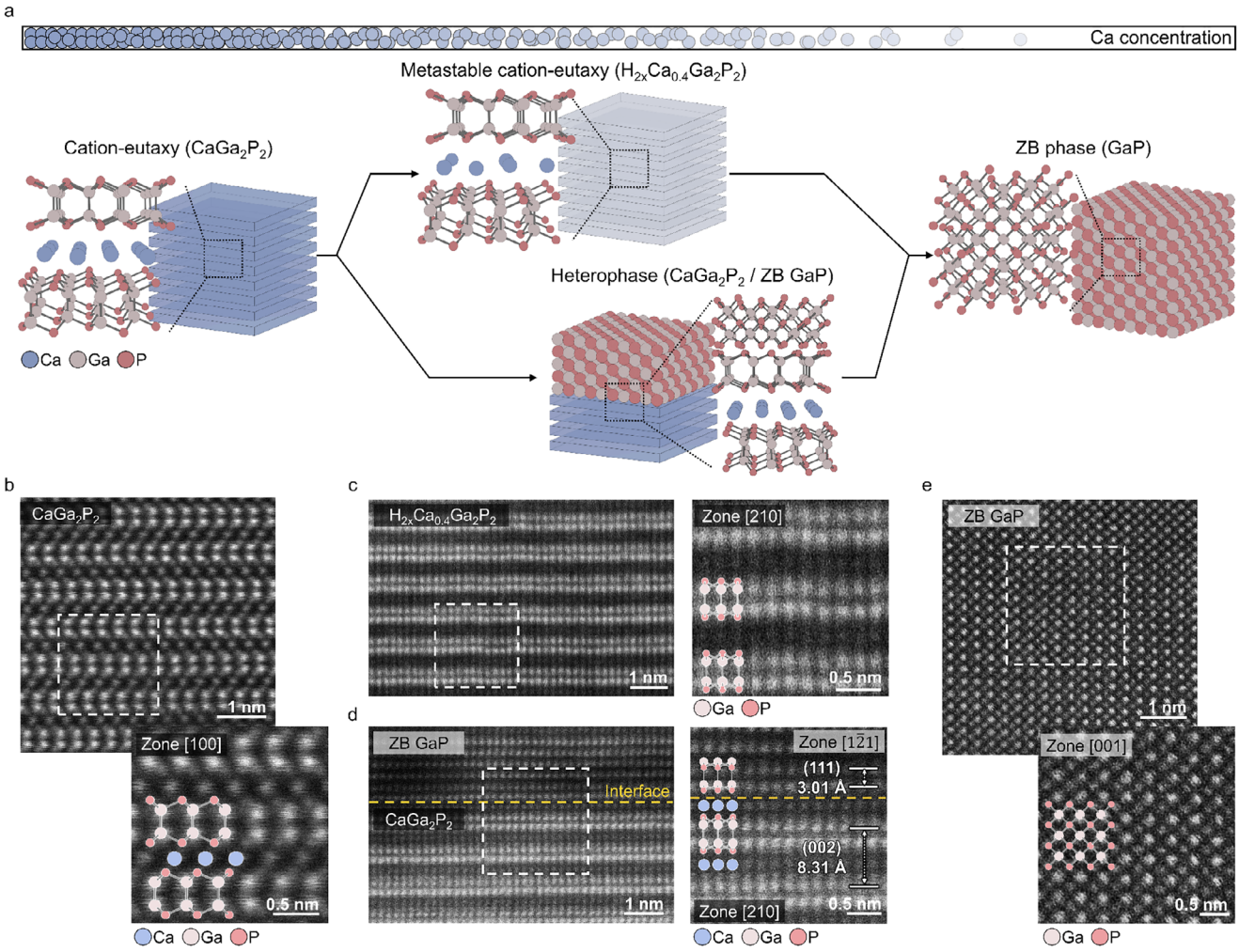

FIGURE 2 | Ca composition-dependent structural evolution of $CaGa_2P_2$. (a) Schematic overview of the structural states that emerge as Ca is progressively removed from $CaGa_2P_2$: the stable cation-eutaxy phase, a Ca-deficient metastable cation-eutaxy phase, a $CaGa_2P_2$/ZB GaP heterophase, and the final ZB GaP phase. (b) HAADF–STEM image (top left) and enlarged image (bottom right) of pristine $CaGa_2P_2$ viewed along [100] zone axis, showing the ordered cation-eutaxy framework with alternating Ca and [GaP] layers. (c) HAADF–STEM image (left) and enlarged image (right) of $H_{2x}Ca_{0.4}Ga_2P_2$ viewed along [210] zone axis, confirming preservation of the layered framework despite reduced Ca occupancy. (d) HAADF–STEM image (left) and enlarged image (right) of $Ca_{0.3}Ga_2P_2$ sample exhibiting a $CaGa_2P_2$/ZB GaP heterophase. The atomically sharp interface between ZB GaP (111) and $CaGa_2P_2$ (001) planes is highlighted, together with the corresponding [1$\bar{2}$1]/[210] zone axis views. (e) HAADF–STEM image (top left) and enlarged image (bottom right) of fully Ca removed ZB GaP. The area marked with a white box indicates the region of the enlarged image.

In $H_{2x}Ca_{0.4}Ga_2P_2$, the $[Ga_2P_2]^{2-}$ layers remain intact, while Ca column intensity decreases (Figure 2c). Projection along the [210] zone axis confirms that the atomic registry is preserved despite Ca deficiency, indicating a metastable cation-eutaxy single phase.

In $Ca_{0.3}Ga_2P_2$, HAADF–STEM reveals spatially separated $CaGa_2P_2$ and ZB GaP domains (Figure 2d), with compositional separation confirmed by TEM–EDS (Figure S2a,b). The EDS line-scan analysis further shows an abrupt compositional discontinuity across the interface (Figure S2c–e). The two phases meet at a flat, atomically sharp interface that maintains continuous atomic registry over ≈18.5 nm, as confirmed by HAADF–STEM (Figure S3; Note S1). The (001) plane of $CaGa_2P_2$ aligns epitaxially with the (111) plane of ZB GaP, minimizing lattice misfit (Figure S4) [29, 30]. Because the lattice misfit between the $CaGa_2P_2$ (001) and ZB GaP (111) planes is ≈0.26%, the associated elastic strain energy is minimized (Note S2). Such a small misfit reduces the interfacial energy and stabilizes coherent or semi-coherent interfaces [31–33]. Atomic resolution images reveal continuous registry between Ca columns in $CaGa_2P_2$ and P columns in ZB GaP.

When Ca is nearly completely removed, the structure fully transforms into a ZB GaP single phase (Figure 2e). Only cubic atomic column arrangements remain, and no cation-eutaxy motifs or interfacial features are detected. It should be noted that the Ca contents of 0.4 and 0.3 do not represent sharp compositional boundaries; rather, the observation of a metastable cation-eutaxy single phase at $H_{2x}Ca_{0.4}Ga_2P_2$ and separated $CaGa_2P_2$ and ZB GaP domains at $Ca_{0.3}Ga_2P_2$ serves as representative examples of distinct structural states that emerge over a finite and sample-dependent composition range.

2.3 | Bulk-Scale Structural Evolution of $CaGa_2P_2$ Driven by Ca Composition Change

Bulk structural evolution induced by Ca removal is consistent with the atomic-scale observations. Pristine $CaGa_2P_2$ exhibits X-ray diffraction (XRD) patterns that correspond to the $P6_3/mmc$ space group. Rietveld refinement confirms a well-ordered cation-eutaxy single phase throughout the bulk (Figure 3a; Table S1). High resolution (HR)–TEM acquired along the [210] zone axis reveals uniform layer stacking over extended length scales (Figure 3b, left). The measured (002) plane spacing (d) is d_{002} = 8.33 Å (Figure 3b, middle). Selected area electron diffraction (SAED) patterns show reflections at d = 8.47 Å for (002) plane and d = 1.95 Å for (1$\bar{2}$0) plane, in agreement with hexagonal reciprocal geometry (Figure 3b, right).

$H_{2x}Ca_{0.4}Ga_2P_2$ preserves the same hexagonal symmetry at the bulk scale. XRD peak positions remain nearly identical to those of pristine $CaGa_2P_2$, whereas the relative intensity ratio of the (002) and (107) reflections changes due to reduced Ca site occupancy (Figure S5) [34]. Rietveld refinement attributes this change to partial Ca depletion rather than structural collapse (Figure 3c; Table S2). HR–TEM yields a reduced interlayer spacing of d_{002} = 8.16 Å, which reflects a slight contraction of the layered framework (Figure 3d) [35]. SAED patterns continue to exhibit hexagonal symmetry (Figure 3d, right).

At $Ca_{0.3}Ga_2P_2$, bulk diffraction reveals the coexistence of $CaGa_2P_2$ ($P6_3/mmc$) and ZB GaP ($F\bar{4}3m$). Rietveld refinement yields a weight fraction of 17:83 for $CaGa_2P_2$ and ZB GaP, respectively (Figure 3e; Table S3) [36]. We note that XRD alone cannot directly confirm the presence of hydrogen in the sample. Further investigation using proton nuclear magnetic resonance (^{1}H NMR) will be required to determine the presence and role of proton species. HR–TEM resolves lattice fringes corresponding to d_{002} = 8.32 Å for $CaGa_2P_2$ and d_{111} = 3.26 Å for ZB GaP within the same region (Figure 3f). SAED pattern displays simultaneous hexagonal and cubic reflections, confirming heterophase coexistence at the bulk scale (Figure 3f, right). Furthermore, we confirmed that the heterophase interface remains stable after annealing at 200°C for 2 h (Figure S6; Table S4).

Near-complete Ca removal drives the structural transition to completion, yielding a ZB GaP single phase. XRD patterns correspond exclusively to the $F\bar{4}3m$ structure, and no reflections associated with $CaGa_2P_2$ are detected (Figure 3g; Table S5). HR–TEM acquired along the [1$\bar{2}$1] zone axis gives a lattice spacing of d_{111} = 3.28 Å (Figure 3h) [37]. SAED pattern shows reflections at d = 3.18 Å for (111) plane and d = 1.66 Å for ($\bar{3}$1$\bar{1}$) plane (Figure 3h, right). The angle between these reflections is approximately 121.5°, which matches the reciprocal geometry of ZB GaP.

2.4 | Structural Evolution Pathways of Ca–III–V Compounds Toward ZB InP and GaAs

To examine the generality of this mechanism, analogous experiments were performed on $CaIn_2P_2$ and $CaGa_2As_2$ (Figure 4a). Phase diagrams indicate that only the cation-eutaxy ternary phase and the ZB III–V phase are thermodynamically stable in both systems (Figure S7) [16]. TEM–EDS confirms the average compositions of all samples (Figures S8; S9).

Pristine $CaIn_2P_2$ exhibits a fully ordered cation-eutaxy structure (Figure 4b). HAADF–STEM shows weak Ca contrast, while an annular bright field (ABF)–STEM imaging confirms full Ca occupancy [38]. SAED reflections at d = 8.74 Å for (002) plane and 2.08 Å (1$\bar{2}$0) plane form an approximately 90° angle, consistent with hexagonal symmetry. $H_{2x}Ca_{0.4}In_2P_2$ retains the cation-eutaxy framework with reduced Ca intensity (Figure 4c). Below the critical Ca concentration, $CaIn_2P_2$ and ZB InP coexist, forming atomically sharp interfaces between the (001) plane of $CaIn_2P_2$ and the (111) plane of ZB InP (Figure 4d and Figure S10). Complete Ca removal yields ZB InP (Figure 4e).

$CaGa_2As_2$ exhibits the same evolution. Pristine $CaGa_2As_2$ shows a well-ordered cation-eutaxy structure with strong Ga–As contrast (Figure 4f). Partial Ca removal yields $H_{2x}Ca_{0.4}Ga_2As_2$ without framework collapse (Figure 4g). At lower Ca content, $CaGa_2As_2$ and ZB GaAs coexist, forming atomically sharp interfaces between the $CaGa_2As_2$ (001) plane and the ZB GaAs (111) plane (Figure 4h; Figure S11). Complete Ca removal yields ZB GaAs (Figure 4i).

These observations demonstrate that the Ca-driven structural evolution from a metastable cation-eutaxy phase to an atomically sharp cation-eutaxy/ZB heterophase is not unique to $CaGa_2P_2$ but recurs consistently in $CaIn_2P_2$ and $CaGa_2As_2$. The reproducible formation of atomically sharp interfaces along the cation-eutaxy (001) planes and the ZB (111) planes establishes this transition pathway as a general characteristic of cation-eutaxy A–III–V compounds rather than a material-specific anomaly.

3 | Conclusion

This work provides an atomic scale description of Ca composition-driven structural evolution in cation-eutaxy A–III–V compounds. Using $CaGa_2P_2$ as a model system, we identify a sequential transition pathway from a stable cation-eutaxy phase to a metastable Ca-deficient cation-eutaxy phase, followed by formation of an atomically sharp cation-eutaxy/ZB heterophase and ultimate conversion to a ZB III–V single phase. The formation of abrupt interfaces under solution-based etching conditions arises from the absence of thermodynamically stable intermediate phases, the large mixing enthalpy imposed by coordination mismatch, and the strong curvature-driven interface flattening force associated with directional III–V covalent bonding. The same transition pathway is reproduced in $CaIn_2P_2$ and $CaGa_2As_2$, demonstrating the generality of this mechanism across the cation-eutaxy A–III–V family. More broadly, the ability to generate atomically sharp heterophase interfaces through composition-controlled transformations offers a new route for designing semiconductor heterostructures beyond conventional epitaxial growth. Such abrupt interfaces can minimize interfacial disorder and enable well-defined band alignment and carrier confinement, which are advantageous for electronic and optoelectronic devices. These findings therefore suggest a potential pathway for

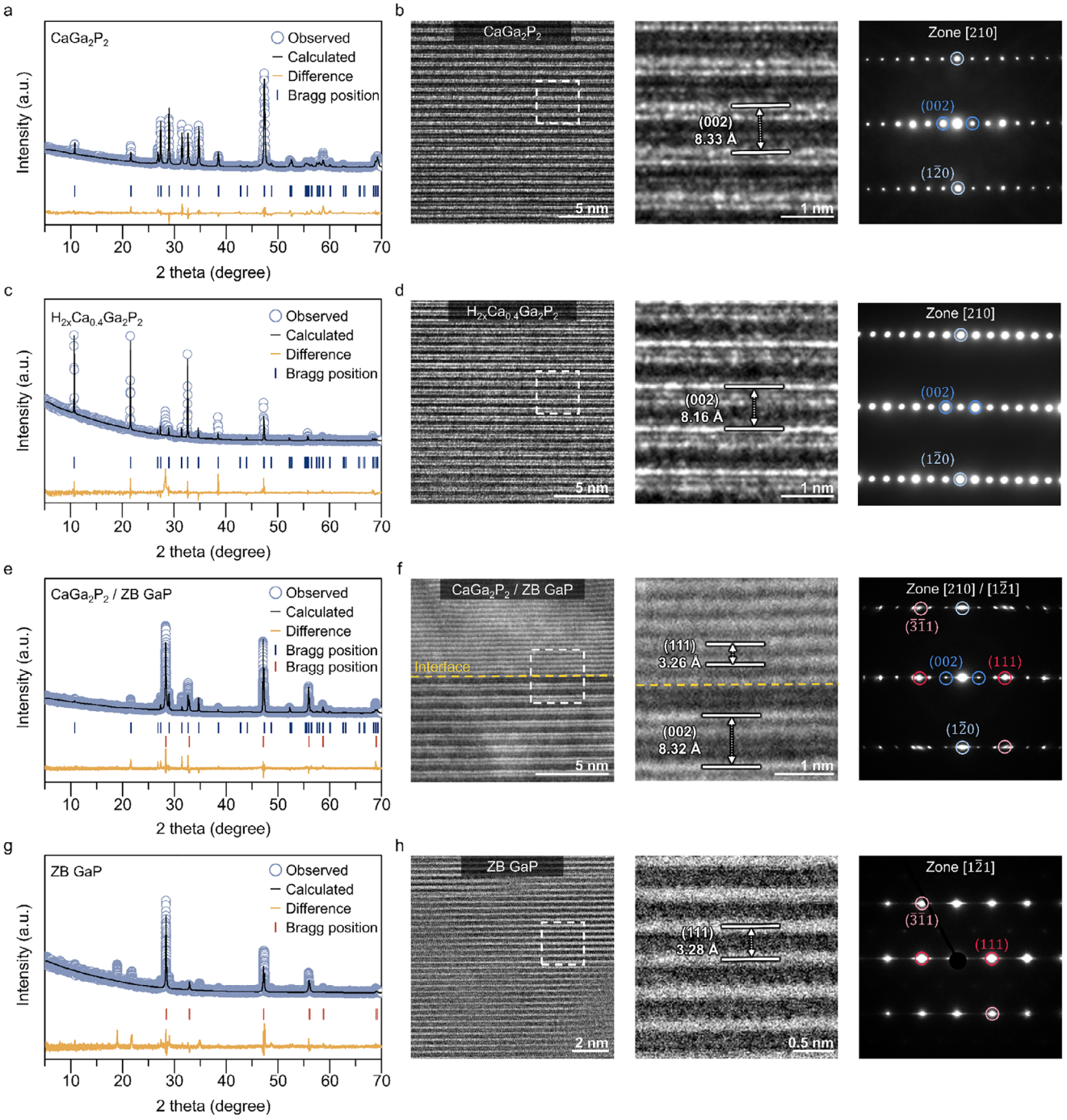

FIGURE 3 | Bulk-scale structural evolution of $CaGa_2P_2$ as a function of Ca composition. (a) Rietveld refined the XRD pattern of pristine $CaGa_2P_2$. (b) HR–TEM image (left), enlarged image (middle), and the SAED pattern (right) along the [210] zone axis of pristine $CaGa_2P_2$. (c) Rietveld refined the XRD pattern of $H_{2x}Ca_{0.4}Ga_2P_2$. XRD pattern shows a single metastable cation-eutaxy phase, with intensity variations attributed to reduced Ca occupancy compared to pristine $CaGa_2P_2$. (d) HR–TEM image (left), enlarged image (middle), and the SAED pattern (right) along the [210] zone axis of $H_{2x}Ca_{0.4}Ga_2P_2$. HR–TEM shows preserved layered stacking with a slightly contracted interplanar spacing of (002) plane. (e) Rietveld refined XRD pattern of $Ca_{0.3}Ga_2P_2$. Rietveld refinement revealed the coexistence of cation-eutaxy $CaGa_2P_2$ and ZB GaP. (f) HR–TEM image (left), enlarged image (middle), and the SAED pattern (right) of $Ca_{0.3}Ga_2P_2$. HR–TEM image shows an atomically abrupt interface between $CaGa_2P_2$ and ZB GaP. The SAED pattern displays coexisting hexagonal and cubic reflections. (g) Rietveld refined XRD pattern of ZB GaP. The XRD pattern shows the ZB GaP structure with no remaining $CaGa_2P_2$ signatures. (h) HR–TEM image (left), enlarged image (middle), and the SAED pattern (right) along the [1$\bar{2}$1] zone axis of ZB GaP. The area marked with a white box indicates the region of the enlarged image.

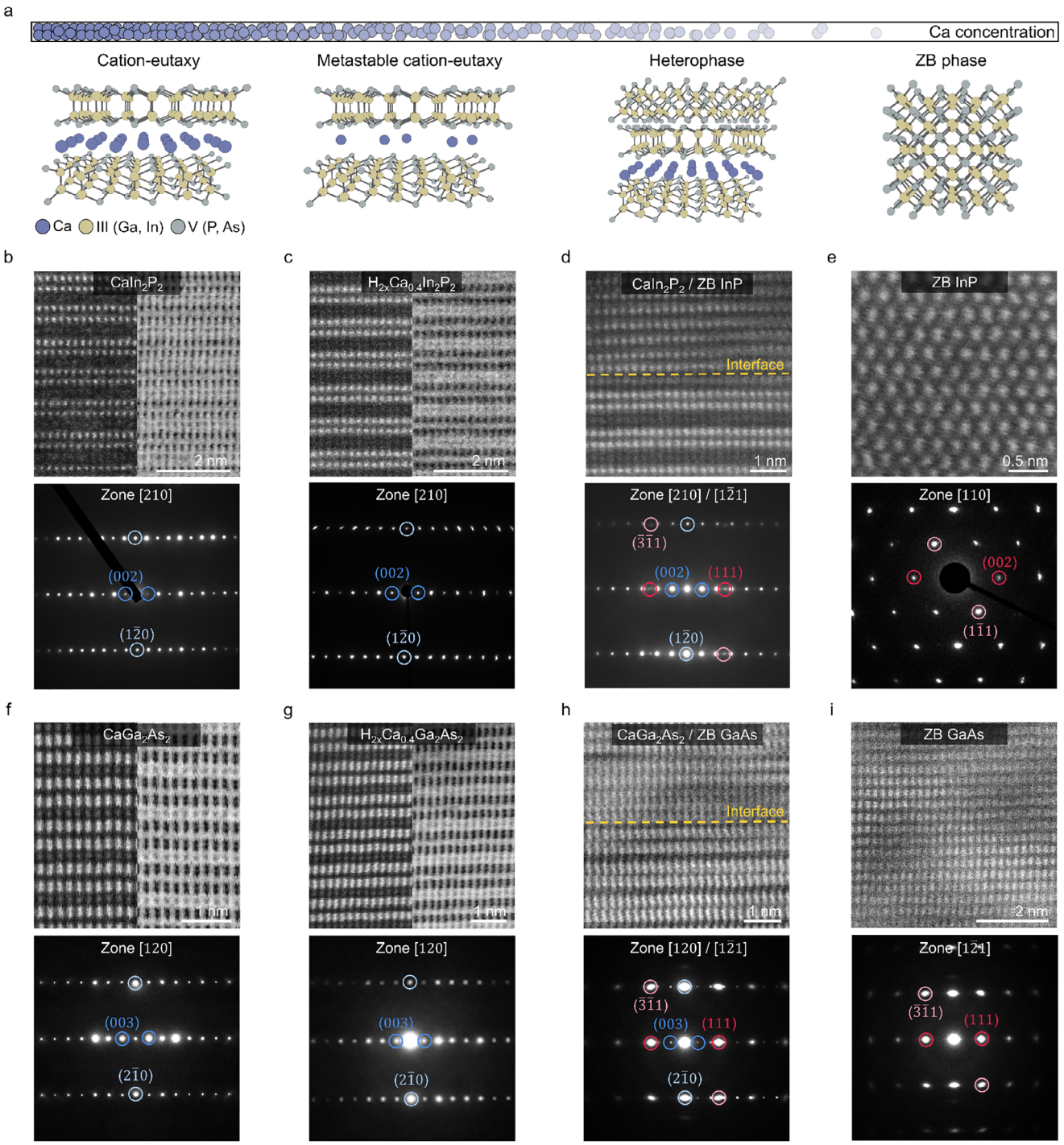

FIGURE 4 | Composition-driven structural evolution pathways of Ca–III–V compounds. (a) Representative structural models illustrating the cation-eutaxy phase, metastable cation-eutaxy phase, heterophase, and ZB III–V phase. (b) HAADF–STEM image (top left), ABF–STEM image (top right), and SAED pattern (bottom) of $CaIn_2P_2$. (c) HAADF–STEM image (top left), ABF–STEM image (top right), and SAED pattern (bottom) of $H_{2x}Ca_{0.4}In_2P_2$. ABF–STEM image shows reduced Ca column contrast while retaining hexagonal symmetry. (d) HAADF–STEM image (top) and SAED pattern (bottom) of $CaIn_2P_2$/ZB InP heterophase. HAADF–STEM image shows an atomically sharp interface, and SAED pattern reveals coexisting hexagonal and cubic reflections. (e) HAADF–STEM image (top) and SAED pattern (bottom) of ZB InP. (f) HAADF–STEM image (top left), ABF–STEM image (top right), and SAED pattern (bottom) of $CaGa_2As_2$. (g) HAADF–STEM image (top left), ABF–STEM image (top right), and SAED pattern (bottom) of $H_{2x}Ca_{0.4}Ga_2As_2$ retaining layered stacking with reduced Ca column contrast. (h) HAADF–STEM image (top) and SAED pattern (bottom) of a $CaGa_2As_2$/ZB GaAs heterophase. HAADF–STEM image shows an abrupt interface, and SAED pattern shows both hexagonal and cubic diffraction spots. (i) HAADF–STEM image (top) and SAED pattern (bottom) of ZB GaAs.

creating high-quality heterostructures through solution-based processes.

4 | Methods

4.1 | Synthesis of $CaGa_2P_2$ and Ca Composition-Controlled Ga–P Derivatives

$CaGa_2P_2$ was synthesized by a conventional solid-state reaction using high-purity elemental precursors. All handling steps, except sealing, were conducted in an inert Ar-filled glovebox to avoid Ca oxidation. Calcium granules, gallium metal, and red phosphorus were loaded into an alumina crucible in the appropriate stoichiometric ratio, sealed in an evacuated quartz ampoule, and heated in a programmable furnace. The mixture was first heated to 150°C for 1 h and held for 5 h to dissolve Ga, followed by heating to 900–920°C for 10 h, maintaining this temperature for 40 h, and slow cooling to room temperature over ≈200 h. The resulting $CaGa_2P_2$ crystals were collected, washed with deionized (DI) water to remove soluble byproducts, and dried. Calcium-deficient $Ca_{1-x}Ga_2P_2$ derivatives were obtained through solution-based Ca etching. $CaGa_2P_2$ powder (≈0.05 g) was immersed in 30% aqueous HNO_3 under ambient conditions, and the Ca content was tuned by controlling the reaction time. A 30 min etching yielded $H_{2x}Ca_{0.4}Ga_2P_2$; a 1 h treatment generated a mixed $CaGa_2P_2$/ZB GaP heterophase; and a 2 h etching produced phase-pure ZB GaP through complete Ca removal. Products were repeatedly washed with DI water to remove $Ca(NO_3)_2$ residues and dried under vacuum.

4.2 | Synthesis of $CaIn_2P_2$ and Ca Composition-Controlled In–P Derivatives

$CaIn_2P_2$ was prepared via solid-state synthesis. Calcium dendritic pieces, indium shot, and red phosphorus lumps were loaded into an alumina crucible in the appropriate stoichiometric ratio, sealed in an evacuated quartz ampoule, and heated to 150°C for 1 h and held for 5 h to dissolve indium. The temperature was then raised to 920°C, maintained for 40 h to form the cation-eutaxy $CaIn_2P_2$ phase, and slowly cooled to room temperature over 200 h. The resulting crystals were collected and washed with DI water. Ca-deficient $Ca_{1-x}In_2P_2$ compositions were obtained by solution-based Ca etching. $CaIn_2P_2$ powder (0.05 g) was immersed in 5 mL of 30% aqueous HNO_3, and the Ca content was controlled via etching time: a 30 min treatment produced $H_{2x}Ca_{0.4}In_2P_2$; a 1 h etching yielded a $CaIn_2P_2$/ZB InP heterophase; and a 2 h etching led to complete Ca removal, producing phase-pure ZB InP. After etching, samples were washed thoroughly with DI water, replacing the water twice, to remove $Ca(NO_3)_2$ and residual acid, then dried under vacuum.

4.3 | Synthesis of $CaGa_2As_2$ and Ca Composition-Controlled Ga–As Derivatives

$CaGa_2As_2$ was synthesized using a self-flux solid-state method. Calcium granules, gallium metal, and arsenic powder were mixed in a Ca:Ga:As molar ratio of 3:10:3 under an inert Ar atmosphere, sealed in an evacuated quartz ampoule, heated to 1000°C for 20 h, and slowly cooled to room temperature. Crystals were separated mechanically, and excess Ga flux was removed by repeated centrifugation. Residual byproducts were eliminated by soaking the crystals in an isopropylamine hydrochloride/ethanol solution, followed by ethanol rinsing and drying. Controlled Ca removal was achieved using a saturated aqueous $GaCl_3$ solution mixed with 10% HNO_3 as the etchant. $CaGa_2As_2$ powder was immersed under ambient conditions, and Ca composition was tuned via etching duration. A 1 h treatment produced $H_{2x}Ca_{0.4}Ga_2As_2$; a 1.5 h treatment yielded a $CaGa_2As_2$/ZB GaAs heterophase; and a 3 h etching resulted in complete Ca removal, forming phase-pure ZB GaAs. The products were washed thoroughly with DI water to remove $Ca(NO_3)_2$-containing byproducts and dried under vacuum.

4.4 | HR–TEM and STEM Analysis

HR–TEM and SAED analyses were performed using a JEM-2100Plus microscope (JEOL) operated at 200 kV. TEM specimens were prepared in an Ar-filled glovebox by gently crushing crystals in methanol and dropping the resulting suspension onto 400-mesh carbon-coated Cu grids, which were then dried under ambient conditions. Samples for HAADF–STEM and ABF–STEM were prepared using a focused ion beam (FIB) instrument (JIB-4601F, JEOL). STEM imaging and nano-beam/electron diffraction were conducted on a JEM-ARM200F microscope (JEOL) equipped with a probe aberration corrector and operated at 200 kV, with a convergence semi-angle of 20 mrad. HAADF–STEM and ABF–STEM images were acquired simultaneously using nominal detector collection angles of 75–310 mrad (HAADF) and 11–22 mrad (ABF), respectively. Fast Fourier transform (FFT) band-pass filtering was applied to selected HAADF–STEM and ABF–STEM images to enhance the visibility of atomic columns, particularly for lighter elements.

4.5 | X-Ray Diffraction and Rietveld Refinement

Powder XRD patterns were collected using a Rigaku Ultima IV diffractometer equipped with Cu Kα radiation (λ = 1.5418 Å, 40 kV, 150 mA). Samples were finely ground in an Ar-filled glovebox, loaded onto zero-background Si holders, and sealed with Kapton film to minimize air exposure. Diffraction data were acquired in the 2θ range of 5–70° with a step size of 0.02° and a scan rate of 1° min^{-1}. Rietveld refinements were performed using the FullProf Suite. Backgrounds were modeled with a 6–12 term polynomial function, and peak shapes were described using a pseudo-Voigt profile. Scale factors, lattice parameters, peak-shape parameters, zero shift, and atomic positions were refined iteratively until convergence was achieved. Preferred orientation corrections were applied when necessary, using the March–Dollase function. The phase fractions are obtained by evaluating the integral intensities of the simulated peaks, while taking into account the Lorentz-Polarization factor, the structure factor, and the multiplicity from multiple equivalent planes. The quality of fit was evaluated through R_{wp}, R_p, R_{exp}, R_{bragg}, and χ^2 parameters, which consistently indicated excellent agreement between the experimental patterns and the refined structural models.

Author Contributions

S.K., J.W., T.K., and W.S. conceived and designed the research. S.K., J.W., T.K., H.C., and S.P. synthesised the materials and carried out structural characterisations. Y.J.C., J.C., and J.-H.L. contributed to data analysis and interpretation. All authors discussed the results and contributed to the final scientific interpretation of the study.

Acknowledgements

This work was supported by the Nano & Material Technology Development Program through the National Research Foundation (NRF) of Korea, funded by the Ministry of Science and ICT (RS-2024-00468995) and a grant from the Institute for Basic Science (IBS-R026-D1).

Conflicts of Interest

The authors declare no conflicts of interest.

Data Availability Statement

The data that support the findings of this study are available from the corresponding author upon reasonable request.

References

1. M. Brahlek, J. Lapano, and J. S. Lee, "Topological Materials by Molecular Beam Epitaxy," *Journal of Applied Physics* 128 (2020): 210902, https://doi.org/10.1063/5.0022948.

2. A. Ron, A. Hevroni, E. Maniv, et al., "Solution Monolayer Epitaxy for Tunable Atomically Sharp Oxide Interfaces," *Advanced Materials Interfaces* 4 (2017): 1700688, https://doi.org/10.1002/admi.201700688.

3. P. Rath, J. C. Chai, H. Y. Zheng, and H. Zhu, "A Fixed-grid Approach for Diffusion- and Reaction-Controlled Wet Chemical Etching," *International Journal of Heat and Mass Transfer* 48 (2005): 2140–2149, https://doi.org/10.1016/j.ijheatmasstransfer.2004.12.033.

4. M. Wolthers, "How Minerals Dissolve," *Science* 349 (2015): 1288, https://doi.org/10.1126/science.aad0852.

5. J. Lang, B. Ding, S. Zhang, et al., "Scalable Synthesis of 2D Si Nanosheets," *Advanced Materials* 29 (2017): 1701777, https://doi.org/10.1002/adma.201701777.

6. J. Bae, J. Won, T. Kim, et al., "Cation-eutaxy-enabled III–V-derived van der Waals Crystals as Memristive Semiconductors," *Nature Materials* 23 (2024): 1402–1410, https://doi.org/10.1038/s41563-024-01986-x.

7. J. Won, T. Kim, M. Lee, et al., "Mapping Cation-eutaxy Ternary With a Phenomenological Model," *Nature Communications* 16 (2025): 5634, https://doi.org/10.1038/s41467-025-60739-9.

8. W. Shim, "An Approach to Identify and Synthesize Memristive III–V Semiconductors," *Nature Materials* 23 (2024): 1322.

9. M. Lee, T. Kim, W. Jang, et al., "Nontypical Wulff-Shape Silicon Nanosheets With High Catalytic Activity," *Journal of the American Chemical Society* 145 (2023): 22620–22632, https://doi.org/10.1021/jacs.3c07768.

10. J. Won, J. Bae, H. Kim, et al., "Polytypic Two-Dimensional FeAs With High Anisotropy," *Nano Letters* 23 (2023): 11057–11065, https://doi.org/10.1021/acs.nanolett.3c03324.

11. T. Kim, J. Won, J. Bae, et al., "Memristive InAs-Based Semiconductors With Anisotropic Ion Transport," *Advanced Materials* 37 (2025): 2500056, https://doi.org/10.1002/adma.202500056.

12. J. Bae, M. Kim, H. Kang, et al., "Kinetic 2D Crystals via Topochemical Approach," *Advanced Materials* 33 (2021): 2006043, https://doi.org/10.1002/adma.202006043.

13. A. K. Da Silva, R. D. Kamachali, D. Ponge, B. Gault, J. Neugebauer, and D. Raabe, "Thermodynamics of Grain Boundary Segregation, Interfacial Spinodal and Their Relevance for Nucleation During Solid-solid Phase Transitions," *Acta Materialia* 168 (2019): 109–120, https://doi.org/10.1016/j.actamat.2019.02.005.

14. S. Zhao, B. Li, B. A. Remington, et al., "Directional Amorphization of Covalently-bonded Solids: A Generalized Deformation Mechanism in Extreme Loading," *Materials Today* 49 (2021): 59–67, https://doi.org/10.1016/j.mattod.2021.04.017.

15. R. W. Balluffi, S. M. Allen, and W. C. Carter, *Kinetics of Materials*. 1st ed. (John Wiley & Sons, 2005), https://doi.org/10.1002/0471749311.

16. A. Jain, S. P. Ong, G. Hautier, et al., "Commentary: The Materials Project: A Materials Genome Approach to Accelerating Materials Innovation," *APL Materials* 1 (2013): 011002, https://doi.org/10.1063/1.4812323.

17. Y. Tan, J. Li, Z. Tang, J. Wang, and H. Kou, "Design of High-entropy Alloys With a Single Solid-solution Phase: Average Properties vs. their Variances," *Journal of Alloys and Compounds* 742 (2018): 430–441, https://doi.org/10.1016/j.jallcom.2018.01.252.

18. G. Hautier, S. P. Ong, A. Jain, C. J. Moore, and G. Ceder, "Accuracy of Density Functional Theory in Predicting Formation Energies of Ternary Oxides From Binary Oxides and Its Implication on Phase Stability," *Physical Review B* 85 (2012): 155208, https://doi.org/10.1103/PhysRevB.85.155208.

19. T. Seitz, A. Karabulut, R. M. Suzuki, A. Hoffmann, J. Heck, and S. Herres-Pawlis, "The Golden Goal of Entatic state Model Design: Lowering the Internal Reorganization Energy Leads to Exponential Increase in Electron Transfer Rate," *Chemical Communications* 61 (2025): 3684–3687, https://doi.org/10.1039/D4CC06406B.

20. N. Y. Kim, T. Yim, J. H. Song, J.-S. Yu, and Z. Lee, "Microstructural Study on Degradation Mechanism of Layered $LiNi_{0.6}Co_{0.2}Mn_{0.2}O_2$ Cathode Materials by Analytical Transmission Electron Microscopy," *Journal of Power Sources* 307 (2016): 641–648, https://doi.org/10.1016/j.jpowsour.2016.01.023.

21. M. Sathiya, A. M. Abakumov, D. Foix, et al., "Origin of Voltage Decay in High-capacity Layered Oxide Electrodes," *Nature Materials* 14 (2015): 230–238, https://doi.org/10.1038/nmat4137.

22. B. Palmieri, M. Grant, and S. A. Safran, "Prediction of the Dependence of the Line Tension on the Composition of Linactants and the Temperature in Phase Separated Membranes," *Langmuir* 30 (2014): 11734–11745, https://doi.org/10.1021/la502347a.

23. H. He, R. Stearrett, E. R. Nowak, and S. Bobev, "Gallium Pnictides of the Alkaline Earth Metals, Synthesized by Means of the Flux Method: Crystal Structures and Properties of $CaGa_2Pn_2$, $SrGa_2As_2$, $Ba_2Ga_5As_5$, and $Ba_4Ga_5Pn_8$ (Pn = P or As)," *European Journal of Inorganic Chemistry* 2011 (2011): 4025–4036, https://doi.org/10.1002/ejic.201100065.

24. A. Winkelmann and G. Nolze, "Point-Group Sensitive Orientation Mapping of Non-Centrosymmetric Crystals," *Applied Physics Letters* 106 (2015): 072101, https://doi.org/10.1063/1.4907938.

25. L. Liu, L. Xiao, J. Feng, L. Li, S. Esmaeili, and Y. Zhou, "Bonding of Immiscible Mg and Fe via a Nanoscale Fe_2Al_5 Transition Layer," *Scripta Materialia* 65 (2011): 982–985, https://doi.org/10.1016/j.scriptamat.2011.08.026.

26. S. Ji and X. Chen, "Enhancing the Interfacial Binding Strength Between Modular Stretchable Electronic Components," *National Science Review* 10 (2023): nwac172, https://doi.org/10.1093/nsr/nwac172.

27. J. Zhu and L. Brassart, "Stretching Response of a Polymer Chain With Deformable Bonds," *Physical Review Letters* 134 (2025): 218101, https://doi.org/10.1103/PhysRevLett.134.218101.

28. R. Ishikawa, E. Okunishi, H. Sawada, Y. Kondo, F. Hosokawa, and E. Abe, "Direct Imaging of Hydrogen-atom Columns in a Crystal by Annular Bright-field Electron Microscopy," *Nature Materials* 10 (2011): 278–281, https://doi.org/10.1038/nmat2957.

29. T. Yang, X. Chen, W. Li, X. Han, and P. Liu, "First-principles Calculation on the Interfacial Stability, Electronic Structure and Fracture

Mechanism of NbN/AlN Interface," *Materials Today Communications* 40 (2024): 110013, https://doi.org/10.1016/j.mtcomm.2024.110013.

30. T. Nyyssönen, A. A. Gazder, R. Hielscher, and F. Niessen, "Habit Plane Determination From Reconstructed Parent Phase Orientation Maps," *Acta Materialia* 255 (2023): 119035, https://doi.org/10.1016/j.actamat.2023.119035.

31. J. Tersoff and F. K. LeGoues, "Competing Relaxation Mechanisms in Strained Layers," *Physical Review Letters* 72 (1994): 3570–3573, https://doi.org/10.1103/PhysRevLett.72.3570.

32. B. J. Spencer, P. W. Voorhees, and S. H. Davis, "Morphological Instability in Epitaxially Strained Dislocation-free Solid Films," *Physical Review Letters* 67 (1991): 3696–3699, https://doi.org/10.1103/PhysRevLett.67.3696.

33. S.-H. Bae, K. Lu, Y. Han, et al., "Graphene-Assisted Spontaneous Relaxation towards Dislocation-Free Heteroepitaxy," *Nature Nanotechnology* 15 (2020): 272–276, https://doi.org/10.1038/s41565-020-0633-5.

34. G. S. Rohrer *Structure and Bonding in Crystalline Materials* (Cambridge University Press, 2001), https://doi.org/10.1017/CBO9780511816116.

35. H. Li, W. Hua, X. Liu-Théato, et al., "New Insights Into Lithium Hopping and Ordering in $LiNiO_2$ Cathodes During Li (De)Intercalation," *Chemistry of Materials* 33 (2021): 9546–9559, https://doi.org/10.1021/acs.chemmater.1c02680.

36. R. J. Hill and C. J. Howard, "Quantitative Phase Analysis From Neutron Powder Diffraction Data Using the Rietveld Method," *Journal of Applied Crystallography* 20 (1987): 467–474, https://doi.org/10.1107/S0021889887086199.

37. K. Park, J. Lee, D. Kim, et al., "Synthesis of Polytypic Gallium Phosphide and Gallium Arsenide Nanowires and Their Application as Photodetectors," *ACS Omega* 4 (2019): 3098–3104, https://doi.org/10.1021/acsomega.8b03548.

38. S. D. Findlay, N. Shibata, H. Sawada, et al., "Robust Atomic Resolution Imaging of Light Elements Using Scanning Transmission Electron Microscopy," *Applied Physics Letters* 95 (2009): 191913, https://doi.org/10.1063/1.3265946.

Supporting Information

Additional supporting information can be found online in the Supporting Information section.

Supporting File: adfm74983-sup-0001-SuppMat.pdf.